# Self-Gating Effect Induced Large Performance Improvement of ZnO Nanocomb Gas Sensors

Xiaofang Pan, Xi Liu, Amine Bermak, and Zhiyong Fan*

Department of Electronic and Computer Engineering, Hong Kong University of Science and Technology, Clear Water Bay, Kowloon, Hong Kong, China SAR

ABSTRACT Much greater surface-to-volume ratio of hierarchical nanostructures renders them with promising potential for high performance chemical sensing. In this work, crystalline nanocombs were synthesized *via* chemical vapor deposition and fabricated into resistive gas sensors. Particularly, NO_2 sensing performance of these devices has been systematically characterized, showing higher sensitivity as compared to their nanobelt counterparts. Through device simulation,

it was discovered that the teeth part of a nanocomb could serve as a "negative-potential gate" after accumulating electrons captured by surface adsorbed NO_2 molecules. This self-gating effect eventually results in a greater reduction of nanocomb device channel conductance upon NO_2 exposure, as compared to a nanobelt device, leading to a much higher NO_2 detection sensitivity. This study not only sheds light on the mechanism of performance enhancement with hierarchical nanostructures, but also proposes a rational approach and a simulation platform to design nanostructure based chemical sensors with desirable performance.
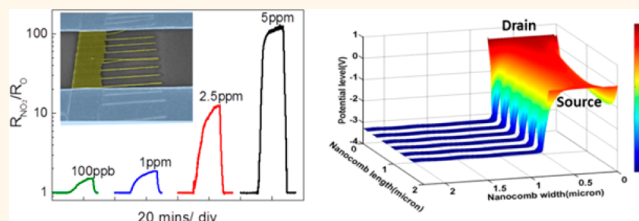
KEYWORDS: nanocomb · hierarchical structure · gas sensor · device simulation · self-gating effect

I n the past decade, gas sensors based on quasi-one-dimensional (Q-1D) semiconducting nanostructures have received tremendous attention because of their improved sensitivity compared with conventional thin film counterparts. Featuring largely increased surface to volume ratio, rich surface chemistry on the nanostructure surfaces effectively alters electrical transport properties of the structures, which can potentially lead to miniaturized chemical and biological sensors with high performance.[1−7] In this regard, diverse strategies have been explored to fabricate chemical sensors based on nanotubes,[8−11] nanowires,[12−15] nanorods,[16,17] nanobelt[18,19] *etc.* Substantial effort has been invested in enhancing their sensing performance, including sensitivity,[20−23] selectivity[24] and long-term reliability.[25] Hierarchical nanostructures are particularly promising candidate materials to further improve sensing performance due to their extremely large surface-to-volume ratio. As a matter of fact, several hierarchical nanostructures have been fabricated into chemical sensors using materials such as ZnO,[26] SnO_2,[27,28] and In_2O_3.[29] In this paper, unique hierarchical ZnO nanocombs have been successfully synthesized with chemical

vapor deposition method. A nanocomb essentially consists of a nanobelt backbone and an array of nanowire teeth, thus featuring high surface area enabling more adsorption of target chemical species. In this paper, these devices were fabricated into two terminal resistive gas sensors and their performance has been systematically characterized. A much higher sensitivity, *e.g.*, 49 times sensitivity for 5 ppm at 200 °C, to NO_2 of nanocombs is observed as compared to the nanobelt-based devices. In addition, device simulation was performed in order to further investigate the origin of the improved sensitivity. By exploring three-dimensional potential distribution across the device, the teeth part of a nanocomb was found to serve as a "negative-potential gate" after accumulating electrons captured by surface adsorbed NO_2 molecules. This "self-gating effect" was found to induce a greater reduction of nanocomb device channel conductance upon NO_2 exposure, as compared to a nanobelt device, leading to a higher NO_2 detection sensitivity.

EXPERIMENTAL RESULTS AND DISCUSSIONS

Characterization of ZnO Nanocomb and Nanobelt. Both ZnO nanocombs and nanobelts

could be successfully fabricated using the vapor trapping Chemical Vapor Deposition (CVD) method (refer to the Fabrication Method section). The quartz vial provides a zinc vapor rich environment (Figure 1a); thus, a gradually decreased zinc/oxygen vapor pressure ratio is formed from the inside vial to the outside. At the bunghole, a small partial vapor pressure difference between zinc and oxygen leads to high nucleation rate so that nanocomb was created due to the polar surface growth. Moreover, nanobelt was found outside of the bunghole, where higher oxygen concentration results in surface reaction's domination in growth.[30] XRD characterizations (Figure S1) of these structures have confirmed that they are all crystalline ZnO nanostructures. The typical SEM image illustrated in Figure 1c clearly shows the hierarchical shape of a single ZnO nanocomb grown at the area inside the bunghole. It is apparent that the ZnO nanocomb is composed of a long backbone ribbon and highly ordered teeth parallel to each other. The teeth of the dendrite exhibit preferred orientations, indicating a preferred growth direction. On average, the ribbon part is around 0.8 μm wide, and the teeth part is around 3 μm long and 0.15 μm wide, with 0.15 μm spacing. Nanobelts were found at the outer area of the silicon chip; they have a close to triangle shape with a base width of 0.8 μm and a height of around 6 μm. Panels d and e of Figure 1 show TEM images for nanobelt and nanocomb, respectively. It is evident from these images that the long axes of nanobelts and nanocombs have the same crystal orientation ([1$\bar{1}$00]), and the teeth of the nanocombs grow along [0001] direction. These observations are consistent with the previous reports.[31,32]

Electronic Properties of ZnO Nanocomb and Nanobelt. To characterize their electronic properties, ZnO nanobelts and nanocombs have been fabricated into back-gated field-effect transistors (FETs) following the fabrication approach reported previously.[33] Figure 2a,b demonstrates the $I-V_{ds}$ curves of the representative nanobelt and nanocomb FET devices, obtained at different gate voltages, with the insets showing the SEM images of the devices. N-type behavior can be seen by the fact that increasing gate voltage leads to the increase of source-drain current. Meanwhile, near-ohmic contact can be also observed, which is manifested by the close to linear $I-V_{ds}$ relationship near zero source-drain bias. Panels c and d of Figure 2 show the transfer characteristics ($I-V_g$) of the nanobelt and nanocomb FETs, respectively, obtained under different drain biases from 0.05 to 0.2 V with a 0.05 V step size. It is apparent that these devices are typical n-channel devices with increasing gate voltage leading to higher channel conductance and they do not show significant difference on the level of ON current. Furthermore, as the nanobelt has a regular geometry, its capacitance (C_{ox}) with respect to the $p++$ back-gate can be easily simulated to be 1.1×10^{-16} F using Finite Element
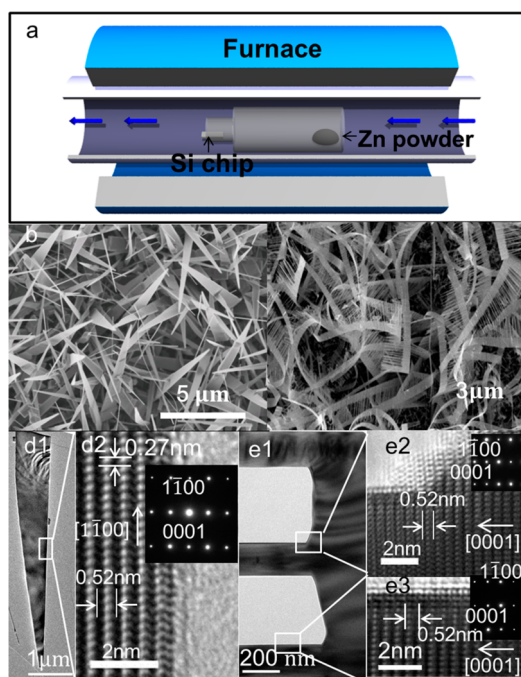

Figure 1. (a) The instrumental setup designed for vapor trapping CVD method is illustrated. The quartz vial is used to create a zinc rich environment. Top-view SEM images of nanobelt (b) and nanocomb (c). TEM images of a nanobelt (d1, d2), nanocomb teeth backbone junction (e1, e2) and its teeth (e3). It is evident that nanobelt and nanocomb produced from this method have an identical crystal orientation.

Method Magnetics (FEMM) program (Figure S2). Therefore, the carrier concentration (n) and field-effect mobility (μ) can be estimated using the following expression:

$$n = \frac{V_{gth}}{e} \times \frac{1}{L \times S} \times C_{ox} = 2.1 \times 10^{16}\,\text{cm}^{-3} \quad (1)$$

$$\mu = (dI/dV_{gs}) \times (L^2/C_{ox}) \times (1/V_{ds}) = 36\,\text{cm}^2/\text{Vs} \quad (2)$$

where dI/dV_{gs} is the transconductance extracted from the linear region of the $I-V_g$ curves, L and S are length and the cross-sectional area of the nanobelts, and V_{gth} is the gate threshold voltage. While nanocomb is not a simple structure, we only estimated the field-effect mobility of the nanocomb device shown in Figure 2b. With the use of the FEMM simulation tool, the capacitance was found to be 1.9×10^{-16} F, and since $V_{gth} = -6.22$ V, $dI/dV_{gs} = 1.28$ nA/V, the field-effect mobility of the nanocomb device is estimated to be

$$\mu = (dI/dV_{gs}) \times (L^2/C_{ox}) \times (1/V_{ds}) = 5.4\,\text{cm}^2/\text{Vs} \tag{3}$$

It can be seen that the nanocomb device has much lower field-effect mobility as compared to the nanobelt device; this can be attributed to larger surface area and more surface defect/dangling bonds which can introduce more carrier scattering.

Gas Sensing Behavior of Nanostructure. The fabricated nanobelt and nanocomb FETs can be readily used as gas sensing devices after wire bonding onto chip
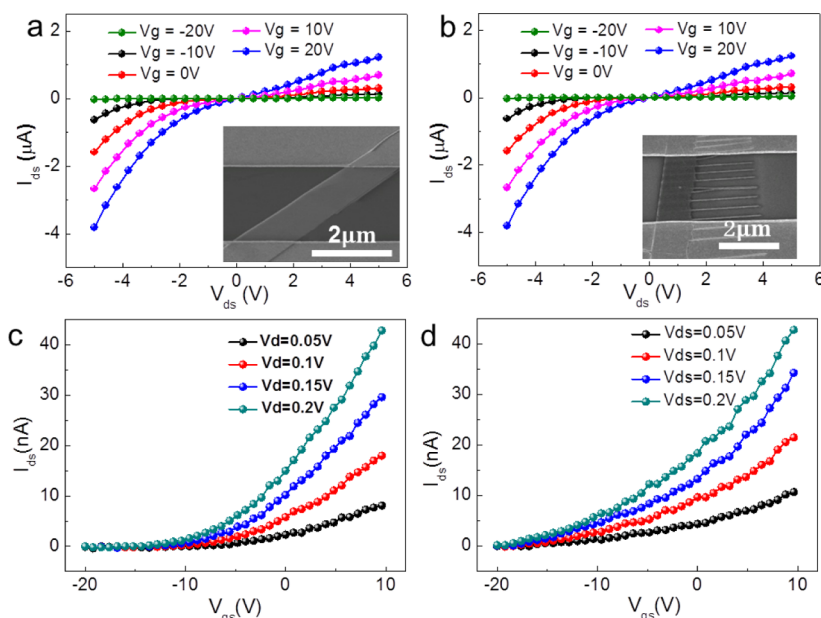
Figure 2. $I_{ds}-V_{ds}$ curves measured from a nanobelt device (a) and a nanocomb device (b). Gate voltage from -20 to 10 V was applied to both devices. The insets are SEM images of nanostructure based back gate FET devices. At four steps of drain voltage, $I_{ds}-V_g$ curves of nanobelt (c) and nanocomb (d) were also measured.

carriers (Figure S4). Gas sensing experiments were carried out in a laboratory experimental platform consisting of a vacuum chamber with electrical feedthroughs, an air pump and a gas delivery system with mass flow controllers (MKS). Before samples were tested, the vacuum system was purged with dry N_2 for 5 min then pumped down to 10^{-3} Torr followed by sample cleaning at 200 °C for 0.5 h in order to remove all the surface adsorbents (primarily H_2O and O_2). Then a series of sensing measurements were conducted at 200 °C with the cover closed. As a result, the experiment was performed in a dark environment without illumination. It is known that UV induces photocurrent in ZnO; therefore, it is necessary to keep the sample in dark condition in the case of laboratory tests. If this sensor is to be deployed for real-life application in which the sensor needs to be exposed to gases and therefore might be exposed to illumination thus introducing a drift in the sensor's response, we intend to solve this issue by designing a read-out circuit with drift/offset cancellation circuitry.

Figure 3 demonstrates time domain response of a typical nanocomb and a nanobelt sensor to NO_2 gas with different concentrations. For the nanocomb sensor, a NO_2 low concentration of 100 ppb already leads to a sensitivity of 1.5 (we define the sensitivity as R_{NO_2}/R_0).[34,35] When the concentration is increased up to 5 ppm, the current is significantly reduced immediately. When the current change is converted to resistance change ratio, the sensitivity is found to be as high as 120. Nanobelt sensor shows a significant resistance change from 2.5 ppm. For 5 ppm NO_2, the nanobelt device sensitivity is estimated as only 2.45 which is much smaller than that of the nanocomb device. Further

increase of the concentration to 10 and 20 ppm results in a nanobelt sensitivity of 4 and 6.8, respectively. Note that the observed sensitivity, especially that of the nanocomb device, does not linearly depend on the concentration. In fact, a power law relationship between sensitivity and concentration is modeled, as shown in Figure S3. This is consistent with various reports from the literature suggesting with experimental and theoretical means that a power law equation is one of the best fit to model the gas sensor sensitivity and concentration relationship.[36-39] For the sake of comparison, it is obvious that the best scenario is to compare the two devices under the same concentration range but unfortunately the two devices feature different dynamic range. Indeed, detection limit of the nanocomb devices is much lower than that of nanobelt one. Therefore, the dynamic range of the nanocomb and the nanobelt devices was set at 0.1—5 ppm and 2.5—20 ppm, respectively. It was found that for the nanobelt device, 20 ppm still cannot completely turn off the channel conductance, which explains the higher setting limit.

Device Simulations. To further highlight the large performance improvement of nanocomb *vs* nanobelt sensors, device simulations using Silvaco (version 5.16.3.R) were performed. In these simulations, adsorption of gas molecules was replaced by surface states. This approach was used to describe the dynamic conductance responses of gas sensors to oxygen as previously reported.[40,41] In general, conductance reduction of ZnO nanowires can be explained using surface vacancy defects model. Namely, oxygen vacancy defects on the nanowire surface help adsorption of oxidizing molecules, which in turn capture free electrons. Equivalently, these vacancy defects function
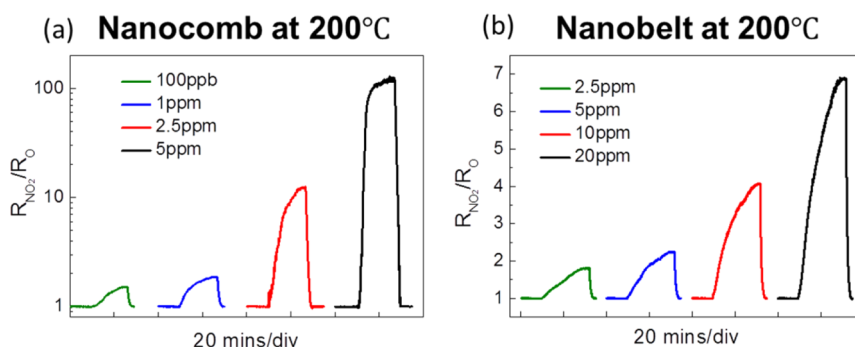
Figure 3. Gas sensing measurement conducted at 200 °C: (a) 0.1, 1, 2.5, and 5 ppm NO$_2$ were applied to the nanocomb device; (b) 2.5, 5, 10, and 20 ppm NO$_2$ were applied to the nanobelt device.

TABLE 1. The Surface State and ZnO Material Related Parameters Adopted in the Simulation[42,44,45]

surface state energy level	surface defects density	electron mobility	hole mobility	electron effective mass	hole effective mass
E_c −1.5 eV	4.8×10^{11} cm^{-2}	100 cm^2/(V s)	34 cm^2/(V s)	$0.24m_0$	$0.8m_0$

as acceptors decreasing free electron concentration. These defect states can also form space charge region and cause band bending near the surface region after capturing electrons.[42] The corresponding parameters in the simulations are listed in Table 1. In this table, surface defect density (4.8×10^{11} cm^{-2}) reflects the density of surface adsorbed molecules, which is expected to have a positive correlation with gas concentration.

The precise geometry of the nanobelt and nanocomb structures used in our simulations can be seen from Figure 4a,b, where dimensions were chosen according to the experimental observation. In all simulations, 0.5 V constant voltage was applied across source and drain electrode and the electrostatic potential distributions in the nanobelt and nanocomb are shown in Figure 4c−f and the conduction band bending are shown in Figure S5a−d. Specifically, Figure 4c,d show potential distributions on the middle cross-sectional planes of a nanobelt cut from nanobelt thickness dimension. panels c and d of Figure 4 show scenarios without and with surface defect states, respectively, simulating the situation of the nanobelt before and after exposure to NO$_2$ gas molecules. It can be seen that the potential of the edge of the nanobelt becomes negative after adsorption of NO$_2$ gas molecules with the lowest potential of −1.16 V near the middle of the nanobelt toward the source, indicating the capture and accumulation of electrons. The edge potential at the location close to source or drain electrode is higher due to the effect of the fixed potential at the source and drain. As electrons can be continuously supplied from source, capturing electrons on nanobelt surface does not directly reduce carrier concentration in the active channel, however, the above observed negative gating effect can lead to regulation of carrier concentration in n-type semiconducting nanobelts, manifested by their reduced conductance. In fact,

negative surrounding gating effect resulted in ZnO nanowire conductance drop has also been observed in optoelectronic study.[43] In both cases, accumulation of electrons is the key factor in reducing the conductance. Furthermore, Figure 4e and f show the potential distributions of a nanocomb before and after exposure to NO$_2$ gas molecules. It is interesting to note that a gradient potential drop was observed from the backbone to the teeth end in Figure 4e. This is due to the fact that ZnO teeth are semiconducting and the bottom substrate below the dielectric is grounded in simulation, while upon exposure to NO$_2$ of the nanocomb device in Figure 4f, large number of electrons are captured and accumulated on the backbone as well as the teeth. Particularly for the teeth part, their relatively small diameter results in a large negative potential of −3.1 V. This negative potential dramatically affects the potential distribution in the backbone of the nanocomb, especially at the junction of the teeth and the nanobelt backbone, as shown in Figure 4f. Overall, this negative self-gating effect has led to lower channel conductance as shown in aforementioned experiments. Meanwhile, I_{ds}−V_{ds} curves of the nanobelt and nanocomb devices were also obtained with simulation shown in Figure S6. It is interesting to observe that the teeth part of the nanocomb does not contribute to conductance as the I_{ds}−V_{ds} curves for nanobelt and nanocomb are almost the same, without surface state/NO$_2$ adsorption. This observation is also consistent with the I−V curves experimentally measured in Figure 2. On the other hand, it is evident that with NO$_2$ adsorption, the conductance of the nanocomb device is about 10 times less than that of the nanobelt device, clearly indicating the strong effect of the charge trapped on surface of the nanocomb teeth part. Beside the surface defect density used in Table 1 (4.8×10^{11} cm^{-2}), two more defect densities, namely, 1×10^{11} and 3.5×10^{11} cm^{-2}, have also been
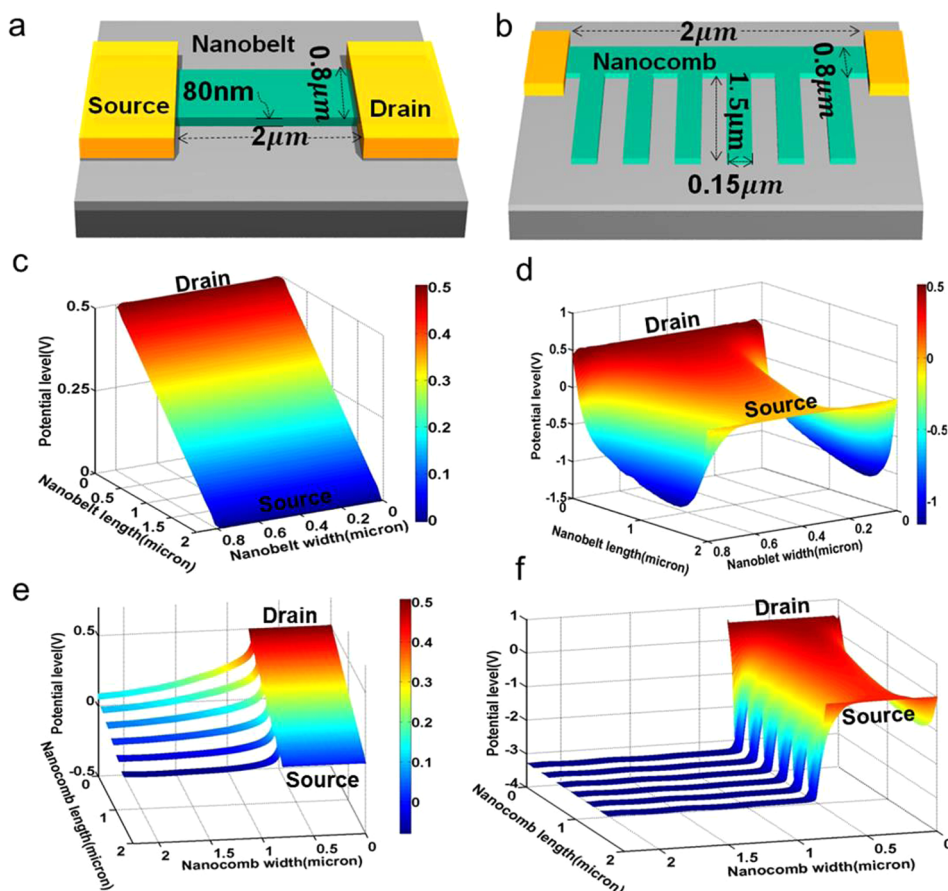
Figure 4. Schematics illustration of morphology parameters adopted in the simulation for nanobelt (a) and nanocomb (b) correspondingly. At 0.5 V drain voltage, (c) and (d) are nanobelt potential distribution without and with NO$_2$ exposure, respectively, and (e) and (f) are nanocomb potential distribution without and with NO$_2$ exposure, respectively.

used for simulation and the simulated $I-V$ curves and device potential distributions are shown in Figure S7. It is conspicuous to note that the conductance of the devices monotonically decreases with increase of surface defect density while the nanocomb teeth potential decreases monotonically with increase of surface defect density as well. These results show a consistent relationship between the surface defect density and the device channel conductance. In the future, the relationship between the surface defect density and the gas concentration needs to be studied, which can provide more accurate prediction/interpretation of experimental measurements and benefit sensor design optimization.

CONCLUSIONS

In summary, we have demonstrated fabrication of nanobelt and nanocomb-based gas sensors, followed by systematic electrical transport characterization and gas (NO$_2$) sensing property investigations of these nanostructures. It was discovered that the hierarchical nanocomb structure substantially outperformed the nanobelt counterpart on sensitivity. Through device simulation, it was revealed that capturing electrons with defects on material surface leads to a negative self-gating effect, which is particularly pronounced for nanocomb devices due to extra surface area. Consequently, this effect resulted in much greater channel conductance reduction upon NO$_2$ exposure for a nanocomb device. These results revealed the mechanism of chemical sensing performance enhancement with hierarchical nanostructures. The paper also outlines an approach to further optimize the nanostructure based chemical sensors using experiments in conjunction with device simulations.

FABRICATION METHOD

ZnO nanobelt and nanocomb were fabricated using our previously developed vapor trapping chemical vapor deposition (CVD) method.[29] Figure 1a demonstrates a schematic of growth configuration. In brief, a 1 cm diameter quartz vial containing 0.3 g of Zn powder (99.9% Sigma-Aldrich) was placed in the middle of the 1 in. quartz tube with the opening end facing down flow of the carrier gas. Such a configuration favors confining Zn vapor locally, thus improving ZnO growth yield. A clean Si was then coated with colloidal gold (Au) nanoparticles with diameter of 30 nm and placed at the bunghole of the small quartz vial. After establishing steady gas flow

with nitrogen at 1 atm pressure, the furnace (Lindberg Blue M) was heated to 700 °C and 100 sccm mixture of oxygen gas and nitrogen gas (N_2/O_2 9:1 v/v) was continually admitted into the furnace for 20 min and then switched back to pure nitrogen followed by natural cooling down of furnace temperature. Eventually, the silicon substrate appears white due to the densely deposition of ZnO nanostructures which were characterized by X-ray diffraction (XRD) (Figure S1), scanning electron microscopy (SEM) and transmission electron microscopy (TEM).

The ZnO nanobelt and nanocomb FETs were fabricated using photolithography followed by microelectrode metallization. Briefly, after ZnO nanostructures growth, the growth chip was ultrasonicated in alcohol to form suspensions of nanomaterial. Then the suspensions were drop-casted onto precleaned Si chips capped with 1 μm thermally grown SiO_2 on the top. Subsequently, LOL 2000 and FH6400L were spin coated onto the chips followed by exposure using SUSS MA6 with a square pad array photolithography mask. After development of the photoresist in FHD-5, bilayer metal contact (10 nm Ti and 90 nm Au) was evaporated onto the chips followed by lift-off in acetone. After the device fabrication process, the devices were annealed at 200 °C for 20 min to improve the contact between nanostructure and electrodes.

Conflict of Interest: The authors declare no competing financial interest.

Supporting Information Available: XRD spectra of ZnO nanocomb and nanobelt are illustrated in Figure S1; schematics of capacitance calculation and electric field distribution generated by FEMM are illustrated in Figure S2; the power law relationship between concentration and sensitivity is presented Figure S3; pictures of nanocomb and nanobelt chips after bonding are illustrated in Figure S4; schematics of conduction band bending without/with NO_2 adsorption for nanobelt and nanocomb are illustrated in Figure S5; $I-V$ curves modeled by Silvaco without/ with NO_2 adsorption for nanobelt and nanocomb are illustrated in Figure S6; simulation results of different surface defect concentrations are illustrated in Figure S7. This material is available free of charge *via* the Internet at http://pubs.acs.org.

Note Added after ASAP Publication: This manuscript was published on the Web on September 4, 2013. Table 1 was corrected and the revised version was reposted on September 12, 2013.

REFERENCES AND NOTES

1. Zheng, G. F.; Patolsky, F.; Cui, Y.; Wang, W. U.; Lieber, C. M. Electrical Detection of Cancer Markers with Nanowire Sensor Arrays. *Nat. Biotechnol.* **2005**, *23*, 1294–1301.
2. He, J. H.; Zhang, Y. Y.; Liu, J.; Moore, D.; Bao, G.; Wang, Z. L. ZnS/Silica Nanocable Field Effect Transistors as Biological and Chemical Nanosensors. *J. Phys. Chem. C* **2007**, *111*, 12152–12156.
3. Sysoev, V. V.; Strelcov, E.; Sommer, M.; Bruns, M.; Kiselev, I.; Habicht, W.; Kar, S.; Gregoratti, L.; Kiskinova, M.; Kolmakov, A. Single-Nanobelt Electronic Nose: Engineering and Tests of the Simplest Analytical Element. *ACS Nano* **2010**, *4*, 4487–4494.
4. Kolmakov, A.; Zhang, Y. X.; Cheng, G. S.; Moskovits, M. Detection of CO and O_2 using Tin Oxide Nanowire Sensors. *Adv. Mater. (Weinheim, Ger.)* **2003**, *15*, 997–1000.
5. Zhang, D. H.; Liu, Z. Q.; Li, C.; Tang, T.; Liu, X. L.; Han, S.; Lei, B.; Zhou, C. W. Detection of NO_2 Down to ppb Levels Using Individual and Multiple In_2O_3 Nanowire Devices. *Nano Lett.* **2004**, *4*, 1919–1924.
6. Kong, J.; Franklin, N. R.; Zhou, C.; Chapline, M. G.; Peng, S.; Cho, K.; Dai, H. Nanotube Molecular Wires as Chemical Sensors. *Science* **2000**, *287*, 622–625.
7. Curreli, M.; Li, C.; Sun, Y.; Lei, B.; Gundersen, M. A.; Thompson, M. E.; Zhou, C. Selective Functionalization of In_2O_3 Nanowire Mat Devices for Biosensing Applications. *J. Am. Chem. Soc.* **2005**, *127*, 6922–6923.
8. Boehme, M.; Voelklein, F.; Ensinger, W. Low Cost Chemical Sensor Device for Supersensitive Pentaerythritol Tetranitrate (PETN) Explosives Detection Based on Titanium Dioxide Nanotubes. *Sens. Actuators, B* **2011**, *158*, 286–291.
9. Gao, R.; Strehle, S.; Tian, B.; Cohen-Karni, T.; Xie, P.; Duan, X.; Qing, Q.; Lieber, C. M. Outside Looking in: Nanotube Transistor Intracellular Sensors. *Nano Lett.* **2012**, *12*, 3329–3333.
10. Zheng, Q.; Zhou, B.; Bai, J.; Li, L.; Jin, Z.; Zhang, J.; Li, J.; Liu, Y.; Cai, W.; Zhu, X. Self-Organized TiO_2 Nanotube Array Sensor for the Determination of Chemical Oxygen Demand. *Adv. Mater. (Weinheim, Ger.)* **2008**, *20*, 1044–1049.
11. Salehi-Khojin, A.; Field, C. R.; Yeom, J.; Masel, R. I. Sensitivity of Nanotube Chemical Sensors at the Onset of Poole–Frenkel Conduction. *Appl. Phys. Lett.* **2010**, *96*, 163110.
12. Cui, Y.; Wei, Q. Q.; Park, H. K.; Lieber, C. M. Nanowire Nanosensors for Highly Sensitive and Selective Detection of Biological and Chemical Species. *Science* **2001**, *293*, 1289–1292.
13. Skucha, K.; Fan, Z.; Jeon, K.; Javey, A.; Boser, B. Palladium/Silicon Nanowire Schottky Barrier Based Hydrogen Sensors. *Sens. Actuators, B* **2010**, *145*, 232–238.
14. Guo, B.; Bermak, A.; Chan, P. C.; Yan, G. A Monolithic Integrated 4 × 4 Tin Oxide Gas Sensor Array with On-Chip Multiplexing and Differential Readout Circuits. *Solid-State Electron.* **2007**, *51*, 69–76.
15. Fan, Z.; Lu, J. G. Gate-Refreshable Nanowire Chemical Sensors. *Appl. Phys. Lett.* **2005**, *86*, 123510.
16. Chien, F. S.; Wang, C.; Chan, Y.; Lin, H.; Chen, M.; Wu, R. Fast-Response Ozone Sensor with ZnO Nanorods Grown by Chemical Vapor Deposition. *Sens. Actuators, B* **2010**, *144*, 120–125.
17. Lu, G.; Xu, J.; Sun, J.; Yu, Y.; Zhang, Y.; Liu, F. UV-Enhanced Room Temperature NO_2 Sensor using ZnO Nanorods Modified with SnO_2 Nanoparticles. *Sens. Actuators, B* **2012**, *162*, 82–88.
18. Fields, L.; Zheng, J.; Cheng, Y.; Xiong, P. Room-Temperature Low-Power Hydrogen Sensor Based on a Single Tin Dioxide Nanobelt. *Appl. Phys. Lett.* **2006**, *88*, 263102.
19. Sadek, A. Z.; Choopun, S.; Wlodarski, W.; Ippolito, S. J.; Kalantar-zadeh, K. Characterization of ZnO Nanobelt-Based Gas Sensor for H_2, NO_2, and Hydrocarbon Sensing. *IEEE Sens. J.* **2007**, *7*, 919–924.
20. He, J.; Ho, C.; Chen, C. Polymer Functionalized ZnO Nanobelts as Oxygen Sensors with a Significant Response Enhancement. *Nanotechnology* **2009**, *20*, 065503.
21. Nah, J.; Kumar, S. B.; Fang, H.; Chen, Y.; Plis, E.; Chueh, Y.; Krishna, S.; Guo, J.; Javey, A. Quantum Size Effects on the Chemical Sensing Performance of Two-Dimensional Semiconductors. *J. Phys. Chem. C* **2012**, *116*, 9750–9754.
22. Liao, L.; Lu, H.; Li, J.; He, H.; Wang, D.; Fu, D.; Liu, C.; Zhang, W. Size Dependence of Gas Sensitivity of ZnO Nanorods. *J. Phys. Chem. C* **2007**, *111*, 1900–1903.
23. Choi, Y.; Hwang, I.; Park, J.; Choi, K. J.; Park, J.; Lee, J. Novel Fabrication of an SnO_2 Nanowire Gas Sensor with High Sensitivity. *Nanotechnology* **2008**, *19*, 095508.
24. Zou, X.; Wang, J.; Liu, X.; Wang, C.; Jiang, Y.; Wang, Y.; Xiao, X.; Ho, J. C.; Li, J.; Jiang, C. Rational Design of Sub-Ppm Specific Gas Sensors Array Based on Metal Nanoparticles Decorated Nanowire Enhancement-Mode Transistors. *Nano Lett.* **2013**, *13*, 3287–3292.
25. Guo, B.; Bermak, A.; Chan, P. C.; Yan, G. An Integrated Surface Micromachined Convex Microhotplate Structure for Tin Oxide Gas Sensor Array. *IEEE Sens. J.* **2007**, *7*, 1720–1726.
26. Zhang, Y.; Xu, J.; Xiang, Q.; Li, H.; Pan, Q.; Xu, P. Brush-Like Hierarchical ZnO Nanostructures: Synthesis, Photoluminescence and Gas Sensor Properties. *J. Phys. Chem. C* **2009**, *113*, 3430–3435.
27. Sysoev, V. V.; Button, B. K.; Wepsiec, K.; Dmitriev, S.; Kolmakov, A. Toward the Nanoscopic "Electronic Nose": Hydrogen *vs* Carbon Monoxide Discrimination with an Array of Individual Metal Oxide Nano- and Mesowire Sensors. *Nano Lett.* **2006**, *6*, 1584–1588.

28. Sysoev, V. V.; Goschnick, J.; Schneider, T.; Strelcov, E.; Kolmakov, A. A Gradient Microarray Electronic Nose Based on Percolating SnO_2 Nanowire Sensing Elements. *Nano Lett.* **2007**, *7*, 3182–3188.

29. Choi, K.; Kim, H.; Lee, J. Enhanced CO Sensing Characteristics of Hierarchical and Hollow In_2O_3 Microspheres. *Sens. Actuators, B* **2009**, *138*, 497–503.

30. Chang, P. C.; Fan, Z. Y.; Wang, D. W.; Tseng, W. Y.; Chiou, W. A.; Hong, J.; Lu, J. G. ZnO Nanowires Synthesized by Vapor Trapping CVD Method. *Chem. Mater.* **2004**, *16*, 5133–5137.

31. Xu, C.; Sun, X. W.; Dong, Z. L.; Yu, M. Self-Organized Nanocomb of ZnO Fabricated by Au-Catalyzed Vapor-Phase Transport. *J. Cryst. Growth* **2004**, *270*, 498–504.

32. Huang, Y.; Zhang, Y.; He, J.; Dai, Y.; Gu, Y.; Ji, Z.; Zhou, C. Fabrication and Characterization of ZnO Comb-Like Nanostructures. *Ceram. Int.* **2006**, *32*, 561–566.

33. Fan, Z. Y.; Wang, D. W.; Chang, P. C.; Tseng, W. Y.; Lu, J. G. ZnO Nanowire Field-Effect Transistor and Oxygen Sensing Property. *Appl. Phys. Lett.* **2004**, *85*, 5923–5925.

34. Jiménez, I.; Cirera, A.; Folch, J.; Cornet, A.; Morante, J. Innovative Method of Pulverisation Coating of Prestabilized Nanopowders for Mass Production of Gas Sensors. *Sens. Actuators, B* **2001**, *78*, 78–82.

35. Leng, J.; Xu, X.; Lv, N.; Fan, H.; Zhang, T. Synthesis and Gas-Sensing Characteristics of WO_3 Nanofibers *via* Electrospinning. *J. Colloid Interface Sci.* **2011**, *356*, 54–57.

36. Dan, Y.; Cao, Y.; Mallouk, T. E.; Evoy, S.; Johnson, A. C. Gas Sensing Properties of Single Conducting Polymer Nanowires and the Effect of Temperature. *Nanotechnology* **2009**, *20*, 434014.

37. Chen, H. T.; Ng, K. T.; Bermak, A.; Law, M. K.; Martinez, D. Spike Latency Coding in Biologically Inspired Microelectronic Nose. *IEEE Trans. Biomed. Circuits Syst.* **2011**, *5*, 160–168.

38. Yamazoe, N.; Shimanoe, K. Theory of Power Laws for Semiconductor Gas Sensors. *Sens. Actuators, B* **2008**, *128*, 566–573.

39. Ng, K. T.; Guo, B.; Bermak, A.;Martinez, D.; Boussaid, F. Characterization of a Logarithmic Spike Timing Encoding Scheme for a 4 × 4 Tin Oxide Gas Sensor Array. Presented at the Eighth IEEE Sensors Conference, Christchurch, New Zealand, October 25−28, **2009**.

40. Lagowski, J.; Sproles, E.; Gatos, H. C. Quantitative Study of the Charge Transfer in Chemisorption; Oxygen Chemisorption on ZnO. *J. Appl. Phys.* **1977**, *48*, 3566–3575.

41. Ding, J.; McAvoy, T. J.; Cavicchi, R. E.; Semancik, S. Surface State Trapping Models for SnO_2-Based Microhotplate Sensors. *Sens. Actuators, B* **2001**, *77*, 597–613.

42. Soudi, A.; Hsu, C.; Gu, Y. Diameter-Dependent Surface Photovoltage and Surface State Density in Single Semiconductor Nanowires. *Nano Lett.* **2012**, *12*, 5111–5116.

43. Fan, Z. Y.; Dutta, D.; Chien, C. J.; Chen, H. Y.; Brown, E. C.; Chang, P. C.; Lu, J. G. Electrical and Photoconductive Properties of Vertical ZnO Nanowires in High Density Arrays. *Appl. Phys. Lett.* **2006**, *89*, 213110–213112.

44. Liao, Z.; Liu, K.; Zhang, J.; Xu, J.; Yu, D. Effect of Surface States on Electron Transport in Individual ZnO Nanowires. *Phys. Lett. A* **2007**, *367*, 207–210.

45. Chen, C. Y.; Retamal, J. R. D.; Wu, I. W.; Lien, D. H.; Chen, M. W.; Ding, Y.; Chueh, Y. L.; He, J. H. Probing Surface Band Bending of Surface-Engineered Metal Oxide Nanowires. *ACS Nano* **2012**, *6*, 9366–9372.